A&A, 706, A92 (2026)
https://doi.org/10.1051/0004-6361/202557876

Astronomy & Astrophysics

The binary ballet: Mapping local expansion around M 81 and M 82

Jenny Wagner[1,2,3,⋆], David Benisty[4,⋆], and Igor D. Karachentsev[5,⋆]

[1] Helsinki Institute of Physics, P.O. Box 64, FI-00014 University of Helsinki, Finland
[2] Academia Sinica Institute of Astronomy and Astrophysics, 11F of AS/NTU Astronomy-Mathematics Building, Roosevelt Rd, Taipei 106216, Taiwan, R.O.C.
[3] Bahamas Advanced Study Institute and Conferences, 4A Ocean Heights, Hill View Circle, Stella Maris, Long Island, The Bahamas
[4] Leibniz-Institut für Astrophysik Potsdam (AIP), An der Sternwarte 16, D-14482 Potsdam, Germany
[5] Special Astrophysical Observatory, Russian Academy of Sciences, Nizhny Arkhyz, Karachai-Cherkessian Republic 369167, Russia

Received 28 October 2025 / Accepted 13 December 2025

ABSTRACT

This study of the M 81 complex and its Hubble flow delivers new and improved tip of the red giant branch (TRGB)-based distances for nine member galaxies, yielding a total of 58 galaxies with high-precision TRGB distances. With those, we perform a systematic analysis of the group's dynamics in the core and its embedding in the local cosmic environment. Our analysis confirms that the satellite galaxies of the M 81 complex exhibit a flattened, planar distribution almost perpendicular to the supergalactic pole, and thus aligned with a larger-scale filamentary structure in the local Universe. We demonstrate that the properties of the group's barycentre are robustly constrained by the two brightest members, M 81 and M 82, and that correcting heliocentric velocities for the solar motion in the Local Group decreases the velocity dispersion of the group. Then applying minor and major infall models, we fit the local Hubble flow to constrain the Hubble constant and the total mass of the M 81 complex. The joint best-fit parameters from both models yield $H_0 = (63 \pm 6)$ km/s/Mpc and a total mass of $(2.28 \pm 0.49) \times 10^{12}\,M_\odot$. We thus arrive at an increased mass estimate compared to prior work but reach a higher consistency with virial ($(2.74 \pm 0.36) \times 10^{12}\,M_\odot$) and projected ($(3.11 \pm 0.69) \times 10^{12}\,M_\odot$) mass estimates. Moreover, our H_0 estimate shows an agreement with Planck, consistent with other TRGB-based local-Universe inferences of H_0 and still within a 2σ agreement with Cepheid-based local-Universe probes.

Key words. galaxies: groups: individual: M 81 – cosmological parameters

1. Introduction

The M 81 galaxy complex stands as one of the most prominent and massive groups in the nearby Universe, providing a critical laboratory for studying galaxy interactions, group dynamics, and the small-scale properties of the Hubble flow (Karachentsev & Kashibadze 2006, 2021). Our study introduces previously unmeasured and improved tip of the red giant (TRGB)-based distances for nine galaxies: M 82, d0944+71, KDG 73, UGC 4483, DDO 53, dw0959+68, HolmII, KKH37, and UGC 6456. Among these, the distance to M 82 is particularly vital for dynamically determining the group's centre of mass, while galaxies like HolmII and UGC 6456, located at distances exceeding 1 Mpc from M 81, provide crucial anchors in the Hubble flow regime. This comparably homogeneous TRGB-based sample is supplemented by seven additional galaxies (JKB83, KDG61em, Clump I, Clump III, HIJASS1021+68, UGC 6451, and SMDG0956+82) with distances newly inferred from other methods; the first six are based on associations with neighbouring members, while the last, SMDG0956+82, relies on the numerical action method (NAM) and is consequently too uncertain for our primary analysis despite its location beyond 1 Mpc. Moreover, the first four are emission sparks that do not contain old stellar populations and HIJASS1021+68 is a starless HI cloud, such that the TRGB-approach cannot be applied to these galaxies.

With this extended and improved dataset based on the Catalog and Atlas of Local Volume Galaxies (see Karachentsev et al. (2013) and references therein), we performed a systematic analysis to determine the position and line-of-sight velocity of the group's centre of mass, employing the four brightest central galaxies (M 81, M 82, NGC 3077, and NGC 2976), finding that M 81 and M 82 alone are sufficient to robustly constrain these properties. We then used all 58 galaxies with precise TRGB-based distances to constrain the Hubble constant, H_0, and the total enclosed mass of the M 81 complex, M, through a detailed Hubble flow analysis. This included a thorough investigation of the impact of key nuisance parameters on the final inferred cosmological and dynamical parameters. Most prominently, these nuisance parameters are the correction of the solar motion in the Local Group and the chosen starting and ending distances for the Hubble flow fit. With our systematic analyses of the local expansion field using all galaxies with TRGB-based distances available, this study provides new, precise benchmarks for testing cosmological models on small scales and for understanding the mass assembly of a major galaxy group in a filamentary embedding.

The paper is organised as follows. Sect. 2 describes the characteristics of the dataset and compares it to the one previously used in Müller et al. (2024) and Wagner & Benisty (2025). Sect. 3 discusses the embedding of the M 81 complex into the local cosmic environment. Sect. 4 presents infall models to estimate the radial velocities of galaxies relative to the group's barycentre and also details the pre-processing of the measurements to apply these models, in particular the bias correction to

⋆ Corresponding authors: wagner@asiaa.sinica.edu.tw; dbenisty@aip.de; idkarach@gmail.com

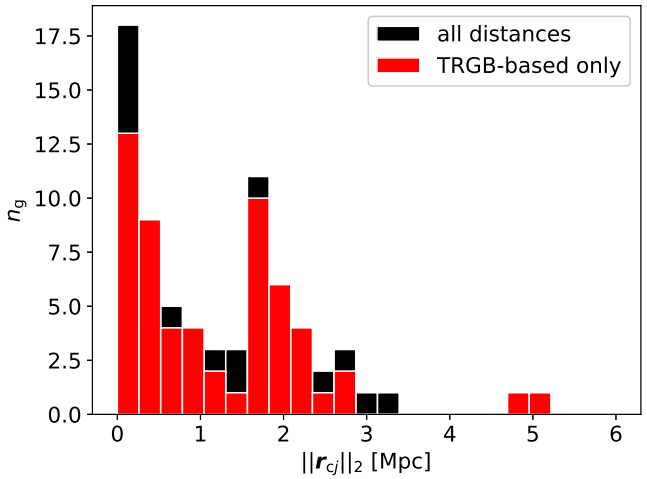

Fig. 1. Histogram of distances for all 71 galaxies with respect to M 81 as the centre (black bars) and only those 57 galaxies that have TRGB-based distances (red bars). The bin size is 0.25 Mpc.

the heliocentric velocities and the determination of the group's barycentre. Then, Sect. 5 details the Hubble flow fitting function and approaches to constrain H_0 and M from our data. Sect. 6 compares the mass estimates from the Hubble flow fit with complementary dynamical mass estimators. Finally, Sect. 7 summarises our results and puts them into the context of prior works and the role of local-Universe Hubble flow fits for the H_0 tension.

2. Dataset

2.1. Dataset description

The total dataset contains 98 galaxies around M 81 and in its embedding environment. Of those, 26 do not have velocity measurements and are excluded from the analysis. Out of the remaining 72 galaxies, 58 have TRGB-based distances, 6 distances were obtained by applying the NAM to galaxies having TRGB-based distances and inferring the distance from the reconstructed dynamical field, as is detailed in Shaya et al. (2017) and Kourkchi et al. (2020), 6 distances were obtained from the galaxy membership in known groups with measured distances of other members (mem), 1 distance was obtained by surface brightness fluctuations (SBF), and 1 distance was obtained based on the texture (txt), i.e. the granular structure of the galaxy (see also Karachentsev et al. (2013) for details). All methods are subject to various calibrations and physical mechanisms, so that their observational uncertainties differ. We assume 5% uncertainties on the TRGB-based distances and estimate the other methods to be 25–30% imprecise.

Fig. 1 shows a histogram of distances around M 81 for all distance measures (black bars) and TRGB-based distances only (red bars) using a binning of 0.25 Mpc. As can be read off this plot, the 58 galaxies that have TRGB-based distances are sufficient to enable us to perform a Hubble flow analysis and we can exclude galaxies with less precise distance measurements from the analysis.

These 58 galaxies with TRGB-based distances were then grouped by finding their 'major disturber' (MD), meaning the closest neighbouring galaxy that exerts the maximum tidal impact on the galaxy, as was detailed in Karachentsev & Makarov (1999). The 'tidal index', Θ_1, for a galaxy, j, to quantify this impact and determine the MD is given by

$$\Theta_1 \equiv \max\left\{\log\left(\frac{M_k}{||r_{jk}||_2}\right)\right\} + C\,, \quad \forall k \neq j\,, \tag{1}$$

in which M_k denotes the mass of the k-th neighbouring galaxy and $||r_{jk}||_2$ denotes the three-dimensional distance between galaxy j and k. The constant, C, was chosen such that $\Theta_1 = 0$ implies that galaxy j lies exactly at the zero-velocity surface of its MD, if the orbit of galaxy j around its MD is Keplerian. Thus, $\Theta_1 \geq 0$ implies that galaxy j is most likely bound to its MD, while $\Theta_1 < 0$ means that galaxy j is unbound, as was also detailed in Karachentsev & Makarov (1999) and Karachentsev et al. (2013).

Grouping the 58 galaxies can now be performed by noting that the six brightest galaxies in the B band are M 81, NGC 2403, M 82, NGC 3077, NGC 2976, and Holm II, with M 81, M 82, NGC 3077, and NGC 2976 being the four central galaxies of the M 81 complex. Uniting those galaxies that have one of these four central galaxies as their MD yields 31 galaxies attributed to the M 81 complex. Only one galaxy, KDG 052, is attributed to Holm II as MD and two galaxies form a system around NGC 2403, DDO 44, and NGC 2366, which have NGC 2403 as their MD. Out of the 31 galaxies in the M 81 complex, five galaxies, all of which have M 81 as their MD, have $\Theta_1 < 0$[1]. Apart from these, there are 14 additional galaxies with other MDs beyond a distance of 1.5 Mpc from M 81 that also have $\Theta_1 < 0$. For each galaxy in our dataset, the B-band magnitude was measured as well. We summarise all information available for the 72 galaxies in Table A.1 in an appendix. To visualise the dataset, we chose supergalactic co-ordinates (see Fig. 2).

2.2. Comparison to our previous dataset

All 21 galaxies of our previous dataset discussed in Wagner & Benisty (2025), originally assembled by Müller et al. (2024), are contained in the new dataset, d1012+64 being called UGC05497. Table A.1 indicates the membership of a galaxy in the Müller et al. (2024) dataset with a star-superscript behind the name of the galaxy. Hence, the 21 galaxies are all at distances of much less than 1 Mpc from M 81.

For KDG 063 and HS 117, no velocities were given in the new dataset. KDG 063 is missing a far-UV flux, so that the previous velocity measurement may be a spurious detection of local Galactic emission. HS 117 shows a far-UV flux, yet only a faint one, requiring a follow-up observation.

The eight satellites in the Müller et al. (2024) dataset beyond the second-turnaround radius of 230 kpc all have Θ_1 values larger or equal than 1.0. So we consider them to be bound to the M 81 complex for now.

3. Embedding in the local environment

To understand the structure of the Hubble flow around the M 81 complex, we analysed its embedding in the local environment. We collected 103 galaxies with TRGB- and SBF-based distances with a distance of less than 8 Mpc from us and 5.12 Mpc around M 81, a supergalactic latitude smaller than 10°, and a supergalactic longitude between 0° and 80° for this task. This

[1] There are six additional galaxies with other distance measures which have $\Theta_1 < 0$, so it may be worth obtaining TRGB-based distances for those.

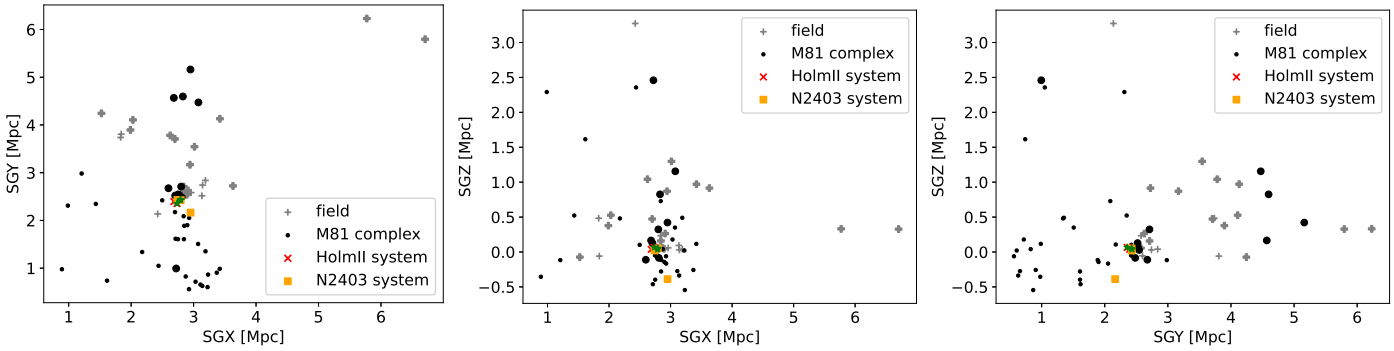

Fig. 2. Locations of the 72 galaxies that have velocity measurements: physical positions in supergalactic co-ordinates in the SGX-SGY-plane (left), SGX-SGZ-plane (centre), and SGY-SGZ-plane (right). Galaxies in the environment are marked as 'field' (grey pluses), galaxies for which M 81, M 82, NGC 3077, or NGC 2976 is the major disturber are summarised under 'M 81 complex' (black dots), the galaxy attributed to Holm II as its major disturber and Holm II itself are called the 'HolmII system' (red xs), and NGC 2403 and two satellites galaxies are called the 'N2403 system' (yellow squares). M 81, Holm II, and NGC 2403 are additionally highlighted by green stars. Larger symbols indicate galaxies that have $\Theta_1 < 0$ and are thus unbound.

sample, restricted to SGL < 65°, is highly complete down to $\log(L_K) = 7.0$. The larger surroundings also point at the mini void behind the M 81 complex as seen from us. Table A.2 lists all of the galaxies used in this section.

In Müller et al. (2024), the flattened structure of the satellite galaxies within a radius of about 250 kpc around the barycentre is studied using the galaxies marked with a star in Table A.1. Additional galaxies (not listed in Table A.1 because they still lack velocity measurements) are also used to constrain the spatial structure of the M 81 complex in Müller et al. (2024). The direction of the smallest extent of the M 81 complex in supergalactic co-ordinates was found to be $\boldsymbol{n} = (-0.1314, +0.0374, +0.9906)$. Excluding four potential outliers, one of which is HS 117, the resulting vector aligns even more with the SGZ axis.

In comparison, we performed a singular value decomposition (SVD) to determine the axes of largest and smallest extent of the larger volume covered by our dataset. To investigate the robustness of the result, we anchored the SVD first around the mean location, then around the median location of all galaxies in Table A.2, and lastly around the centre of mass of the six galaxies with the highest L_K: IC 342, NGC 2403, M 81, NGC 2787, NGC 4258, and NGC 4736. We obtained the direction of smallest extent for the mean of all galaxies as $\boldsymbol{n}_{\rm mean} = (0.0498, -0.1439, 0.9883)$ Mpc, for the median as $\boldsymbol{n}_{\rm median} = (0.0500, -0.1441, 0.9883)$ Mpc, and for the centre of mass of the six most luminous galaxies as $\boldsymbol{n}_{\rm com} = (0.0368, -0.1567, 0.9870)$ Mpc. Thus, the alignment of these directions with respect to the SGZ axis is recovered in the larger volume as well.

Moreover, we also analysed the dependence on the volume covered by the galaxies and the selection of galaxies by restricting the dataset to the 89 galaxies within 3 Mpc from M 81 and to the 34 galaxies within 0.25 Mpc around M 81, which is approximately the volume covered by Müller et al. (2024), yet sampled with slightly different galaxies. While the former yields a good alignment with the previous three directions of smallest extent, $\boldsymbol{n}_{<3\rm Mpc} = (-0.0392, -0.1887, 0.9812)$ Mpc, the inner core is not well aligned anymore with its $\boldsymbol{n}_{<0.25\rm Mpc} = (-0.4602, 0.2073, 0.8633)$ Mpc.

Fig. 3 shows the resulting planes of maximum extent for the entire data volume, the galaxies in a 3 Mpc radius around M 81, and the galaxies in a 0.25 Mpc radius around M 81. As can be read off the plot, and more clearly from the rotating plot in the online movie, the planes become more aligned with increasing volume size. The selection of galaxies by Müller et al. (2024) is already sufficient to arrive at the larger-scale alignment roughly oriented parallel the SGX-SGY plane, in good agreement with many other works detecting sheet-like structures in the local Universe in similar directions; for instance McCall (2014), Anand et al. (2019), or Peebles (2023).

Beyond that, we observe a filamentary structure around the M 81 complex on a smaller scale. This structure is not captured by a single plane, but rather by two filament arms: one from M 81 towards NGC 4258 and another to NGC 4736. The grey plane of maximum extent contains NGC 4258 (also known as M 106, with its water megamaser that has been used extensively to calibrate the cosmic distance ladder; see, for instance, Tully et al. (2023) for a recent discussion), yet it does not contain NGC 4736 (also known as Messier 94) and its satellites. Restricting the volume to a radius of 3 Mpc around M 81 and thereby excluding NGC 4258 and its satellites from the analysis, the red plane is lifted slightly towards NGC 4736 however still does not capture this filamentary part of M 81's environment.

Connecting the local environment of the M 81 complex to the filaments found by Raj et al. (2024), the M 81 complex lies in their 'filament 10', which consists of 63 galaxies, with M 81 (called NGC 3031) marked as the major galaxy in the centre of this filament and Messier 101 (called NGC 5457) at the right end. The next galaxy close to M 81 is NGC 672, attributed to 'filament 0' at the crossing of various filaments. The larger filamentary structure in Raj et al. (2024) seems to share its direction with our grey plane, but occurs on a larger scale. Vice versa, the filamentary structures around the M 81 group captured in our work are on a slightly larger scale than the M 81 satellite alignments found by Müller et al. (2024). On the whole, irrespective of the scale we look at beyond a radius of 0.25 Mpc around M 81, the filaments seem to have a preferred alignment direction approximately perpendicular to the SGX-SGY plane.

4. Galaxy infall models

4.1. Velocity corrections

Before we apply the major and minor infall models, as set up in Karachentsev & Kashibadze (2006), to the velocities of the galaxies, possible corrections for relative mutual motions are in order. The impact of the observers' own motion on the infall models is still an open question to be investigated in this work

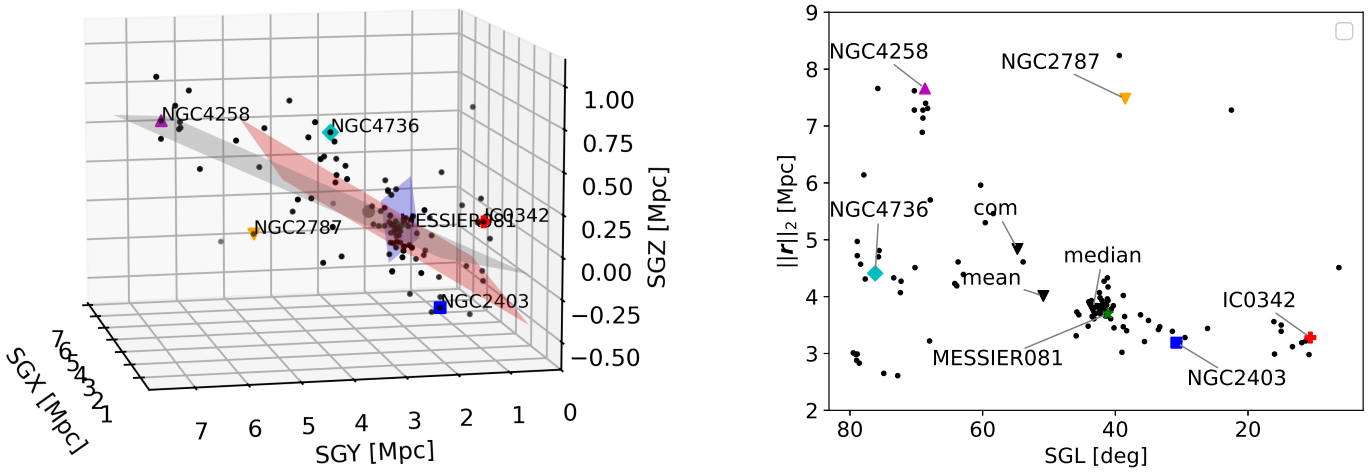

Fig. 3. (Movie online, left plot) Filamentary structure of the local M 81 group including all galaxies of Table A.2. Determining the directions of smallest extent for all 103 galaxies anchored at their mean location, the normal vector to the grey plane was obtained. An analogous calculation for the volume in a 3 Mpc radius around M 81 yielded the red plane and its normal direction. For the volume in the 0.25 Mpc radius around M 81, the blue plane and its normal direction were obtained. The former two planes become more aligned to the SGX-SGY-plane for increasing volume size. For further orientation, the most luminous galaxies in our dataset are marked in colour and their names are attached. The right plot shows a projection into the plane of SGL and the distance from us, and also shows the locations of the mean, median, and centre of mass of the six most luminous galaxies.

M 81 the measured velocities towards galaxies around M 81 contain a contribution of the solar motion with respect to the Milky Way centre and the Milky Way's motion towards the Local Group centre. Assuming that both the M 81 complex and the Local Group move towards the Virgo cluster, correcting the measured velocities for the solar motion within the LG is sufficient to account for the relative motion between us and the M 81 complex.

Thus, we can either use the heliocentric velocities, $v_{\rm hel}$, or take into account the solar motion in the Local Group's gravitational potential. The latter are called $v_{\rm LG}$ in the following. We converted the measured $v_{\rm hel}$ into $v_{\rm LG}$ via

$$v_{\rm LG} = v_{\rm hel} + v_\odot(\sin(b)\sin(b_\odot) + \cos(b)\cos(b_\odot)\cos(l - l_\odot)), \quad (2)$$

in which b and l denote the latitude and longitude of the galaxy in the Galactic co-ordinate system (following the IAU's 1958 definition). For consistency with the data base of Karachentsev et al. (2013), we also used the solar apex with respect to the Local Group rest frame,

$$l_\odot = (93 \pm 2)^\circ\,, \quad b_\odot = (-4 \pm 2)^\circ\,, \quad v_\odot = (316 \pm 5)\ {\rm km/s}, \quad (3)$$

as determined in Karachentsev & Makarov (1996). Although this measurement goes back to the last century, it is still used as a reference for the NASA Extragalactic Database[2] and has been re-measured over the years – for instance, in Tully et al. (2008) or Makarov et al. (2025) – showing a high degree of consistency. When converting $v_{\rm hel}$ to $v_{\rm LG}$, the uncertainties in the solar apex need to be taken into account as well, resulting in larger error bars for the LG-based velocities, as is detailed in the following sections.

4.2. Barycentre of the M 81 complex

Since the M 81 complex is a group of galaxies, we need to determine its barycentre, $\boldsymbol{r}_{\rm c}$, which serves as the centre for all infalling galaxies and the Hubble flow. In Wagner & Benisty (2025), we assumed M 81 to be the barycentre as a first ansatz and considered galaxies within a radial distance of 230 kpc, the extent of the second turnaround radius, to be gravitationally bound. Assuming uncertainties in the distance measures to be 5% for TRGB-based distances and 30% for all other methods, we find that this ansatz is still a good approximation of the true barycentre, because the next three central, brightest galaxies, M 82, NGC 3077, and NGC 2976, all have three-dimensional distances to M 81 that are compatible with zero within their observational uncertainties.

Nevertheless, we investigated a possible refinement of the barycentre position. In Karachentsev & Kashibadze (2006) two different methods were used to determine the barycentre: (1) applying the infall models to all galaxies with respect to a variable $\boldsymbol{r}_{\rm c}$ and determining $\boldsymbol{r}_{\rm c}$ as the location that minimises the velocity dispersion around a Hubble flow fit (see Sect. 5.2); (2) assuming that the mass of the galaxies is proportional to their K-band luminosity, L_K, with the same mass-to-light ratio, $\Upsilon \equiv m_j/L_{Kj}$, for all galaxies, j. This was motivated in Makarov & Karachentsev (2011) and Tully (2015b) by the fact that the observed infrared flux in the local cosmic volume is hardly influenced by dust or young stellar contents, so the same mass-to-light ratio can be used to estimate the stellar mass for all galaxies irrespective of their type and morphology. Assuming that the dark-matter content scales in the same manner, the three-dimensional centre of mass was calculated from the observed angles on the sky and distance,

$$\boldsymbol{r}_{\rm c} = \sum_{j=1}^{n_{\rm g}} \frac{\Upsilon L_{Kj}}{\Upsilon L_{K\rm tot}} \boldsymbol{r}_j, \quad L_{K\rm tot} = \sum_{j=1}^{n_{\rm g}} L_{Kj}, \quad (4)$$

in which $n_{\rm g}$ denotes the number of all galaxies gravitationally bound to the M 81 complex. Since Υ cancels out, we do not require a specific value for the mass-to-light ratio to be known, only the weaker assumption that Υ is the same for all galaxies involved. As is noted in Wagner & Benisty (2025), this formula requires the group's mass to be contained in the galaxies without additional, group-scale dark-matter halos.

Similar to the LG, Karachentsev & Kashibadze (2006) simplified Eq. (4) to only include the two brightest galaxies in the

[2] https://ned.ipac.caltech.edu/help/velc_help.html

group, M 81 and M 82, such that $\boldsymbol{r}_c$ is located on their connection line. We repeated their calculation with the updated observations and also extended the study to the barycentre determined from the four brightest central galaxies in the M 81 complex. We retrieved their K-band luminosities from Karachentsev et al. (2013) as $\log(L_K(\mathrm{M\,81})) = 10.95$, $\log(L_K(\mathrm{M\,82})) = 10.59$, $\log(L_K(\mathrm{N\,3077})) = 9.57$, and $\log(L_K(\mathrm{N\,2976})) = 9.44$. As the central galaxies of the M 81 complex fulfil the small angle approximation, we calculated the line-of-sight velocity component of the barycentre by replacing $\boldsymbol{r}$ by $\boldsymbol{v}_{\mathrm{hel}}$ in Eq. (4). Table 1 summarises all results.

The uncertainties in r_c, the absolute value of the barycentre distance to us, and v_{LGc}, the absolute value of the line-of-sight velocity component corrected for our motion within the LG, were obtained by a linear propagation of uncertainty, taking into account the uncertainties in the line-of-sight distances, line-of-sight velocities, and the uncertainties in the apex parameters when correcting for our motion in the LG. The detailed equations for the propagation of all uncertainties are given in Appendix B.

Lastly, we investigated a varying dark-matter content for the spiral M 81, de Vaucouleurs morphological type 1 or 2, and the spiral but edge-on starburst M 82, de Vaucouleurs morphological type 5, 6, or 7, according to Karachentsev & Kashibadze (2021). Then, $\Upsilon(\mathrm{M\,81}) = (73 \pm 15)\,M_\odot/L_\odot$ and $\Upsilon(\mathrm{M\,82}) = (17.4 \pm 2.8)\,M_\odot/L_\odot$. Calculating the barycentre properties including the varying Υ is summarised in the last row of Table 1. Only the amplitudes and directions of the velocity vectors in the heliocentric and the Local-Group frame change significantly, while the position of the centre still coincides with the one of M 81 within uncertainty bounds.

We thus conclude that the position of the centre of mass remains robustly located at the position of M 81 within the uncertainty bounds. Yet, the v_{hel} of the barycentre changes beyond these limits, which becomes important for the infall models in Sect. 4.3. Only taking into account M 82 as the second-brightest central galaxy is sufficient to constrain the properties of the barycentre under the prerequisites stated above because the properties, including v_{hel}, remain stable when including fainter central galaxies. Allowing for a varying mass-to-light ratio to account for different dark-matter contents of M 81 and M 82 according to heuristics found in Karachentsev & Kashibadze (2021), the velocity vectors tend to align more towards the ones of M 81. Yet, this barycentre does not minimise the velocity dispersion around the Hubble flow as the one with constant Υ does, as was shown in a systematic, dark-matter-model-independent analysis in Karachentsev & Kashibadze (2006). Moreover, determining the barycentre based on a minimisation of the velocity dispersion of the bound galaxies, similar to Karachentsev et al. (2009), we recovered the same barycentre within uncertainty bounds as the one listed in the second row of Table 1 and the one of Karachentsev & Kashibadze (2006). Due to this overall consistency, we thus chose the barycentre that was obtained in the second line of Table 1 in the following.

4.3. Infall models

After defining a centre with respect to which the infall models were calculated and setting up the velocity corrections due to potential biases, we now introduce the infall models that have already been detailed in (Karachentsev & Kashibadze 2006) and Wagner & Benisty (2025). In the following, all infall models approximate the radial velocity component between the centre of mass of the M 81 complex and the surrounding satellite galaxies. To simplify the notation compared to Wagner & Benisty (2025), we denote the absolute values of the line-of-sight distance and velocity components as r and v, respectively. Subscripts c and j denote the group's barycentre and a galaxy j, respectively, such that r_{cj} denotes the absolute value of the three-dimensional distance between the barycentre and galaxy j. The angular distance on the sky between the barycentre and a galaxy, j, is denoted by θ_{cj}. Fig. 4 summarises the notation and directions of vectors.

The **minor infall model** approximates the amplitude[3] of the radial infall velocity of galaxy j onto the barycentre as

$$\left|\boldsymbol{v}_{\mathrm{min}\,j}\right| = \frac{v_c r_c + v_j r_j - \cos\theta_{cj}(v_j r_c + v_c r_j)}{r_{cj}}. \tag{5}$$

This approximation treats the barycentre and galaxy j symmetrically and is an accurate representation of the radial infall velocity if the velocity components perpendicular to the line of sight are negligible.

The **major infall model** is an asymmetric approximation to the radial infall velocity of galaxy j onto the barycentre:

$$\left|\boldsymbol{v}_{\mathrm{maj}\,j}\right| = \frac{v_j - v_c\cos\theta_{cj}}{r_j - r_c\cos\theta_{cj}} r_{cj}\,. \tag{6}$$

It can be derived by projecting the radial velocity onto the infalling galaxy's line of sight. This model becomes an accurate representation of the radial infall velocity for a gravitational bound structure only moving with the cosmic expansion as a whole and containing only radially infalling galaxies. The table included in Fig. 4 lists the accuracy conditions once again.

The angular separation of the galaxies on the sky to the barycentre of the extended M 81 complex is about 44°, such that the small-angle approximation for both infall models by simply subtracting the line-of-sight velocity components of the barycentre and galaxy j is invalid. The latter is only applicable to the galaxies within the second turnaround radius that span a maximum angle of less than 2.3° on the sky, as is detailed in Wagner & Benisty (2025).

As is shown in Wagner & Benisty (2025) and Benisty & Mota (2025) by means of simulations, the minor infall statistically underestimates the radial velocity dispersion, while the major infall is an overestimate of the radial velocity dispersion for most of the groups tested. Applying both infall models to a cosmic structure, lower and upper bounds on the radial velocity dispersion are obtained.

Due to the lack of precise proper motions, only the line-of-sight velocity component was employed, such that the infall models are biased, as is detailed in Wagner & Benisty (2025). Moreover, while three-dimensional distance observations are possible nowadays, the celestial angles on the sky can be measured to a higher precision than the distance along the line of sight. Hence, the major sources of uncertainties in the resulting approximations of the radial infall velocity are the line-of-sight distances.

Fig. C.1 in the appendix shows all galaxy infall velocities for the minor (blue) and major infall models (red) and the simple difference of the line-of-sight velocities as the leading-order approximation to the radial velocity between each galaxy j and M 81, called v_{app} in Wagner & Benisty (2025) (black). The galaxies are sorted according to their three-dimensional distance

[3] Our notation is the same as in Wagner & Benisty (2025), with $|\cdot|$ denoting the signed amplitude of the radial velocity vector with a fixed direction towards the barycentre, a positive sign in this direction and a negative sign otherwise. The absolute value of a vector is defined as $\|\cdot\|_2$.

Table 1. Barycentre determination of the M 81 complex assuming M 81.

Galaxies	α_c [deg]	δ_c [deg]	r_c [Mpc]	Δr_c^* [Mpc]	v_{helc} [km/s]	$\Delta v_{helc}^\dagger$ [km/s]	$d(M\,81)$ [Mpc]	v_{LGc} [km/s]	$\Delta v_{LGc}^\dagger$ [km/s]
M 81	148.889583	69.066667	3.70	0.19	−38	1	0.00	104	10
... & M 82	148.915412	69.253801	3.67	0.14	29	1	0.03	172	10
... & N 3077	148.969617	69.239139	3.68	0.14	29	1	0.03	171	10
... & N 2976	148.925496	69.211995	3.68	0.13	28	1	0.02	171	10
M 81 & M 82	148.897594	69.124703	3.69	0.17	−17	5	0.01	125	11

Notes. Barycentres of the M 81 complex assuming M 81 (first row) and the next three brightest central galaxies (accumulating one galaxy after the other from the second to the fourth row) constrain its position (α_c, δ_c, and the distance, r_c, of the barycentre to us as observers) and its line-of-sight velocity component (v_{helc}). Uncertainties in the distance (Δr_c) and line-of-sight velocity (Δv_{helc}) are given by linear propagation of independent uncertainties. The latter only contain measurement imprecisions and no systematic biases due to potential offsets between dark and luminous matter. The last three columns show the three-dimensional distance between $\boldsymbol{r}_c$ and $\boldsymbol{r}_{M\,81}$, the line-of-sight velocity corrected for the sun's motion in the LG, v_{LG}, and its uncertainty, Δv_{LG}. The last row lists the barycentre properties for a varying mass-to-light ratio; see the text. * determined from distance uncertainties only, assuming 10% or 20% uncertainty in the L_K, changes in Δr_c remain below the precision given here. Uncertainties in the mass-to-light ratio in the last row, as given by Karachentsev & Kashibadze (2021), were taken into account. † determined from distance uncertainties only, assuming 10% uncertainty in the L_K: $\Delta v_{helc} = [1, 7, 7, 6]$ km/s, for 20%, we obtain: $\Delta v_{helc} = [1, 13, 13, 13]$ km/s, analogously for 10% uncertainty in L_K: $\Delta v_{LGc} = [10, 12, 12, 12]$ km/s, for 20%: $\Delta v_{LGc} = [10, 17, 16, 16]$ km/s. Including the uncertainties in the mass-to-light ratio in the last row, assuming additional 10% uncertainty in the L_K: $\Delta v_{helc} = 6$ km/s and $\Delta v_{LGc} = 11$ km/s, and for 20%: $\Delta v_{helc} = 7$ km/s and $\Delta v_{LGc} = 12$ km/s.

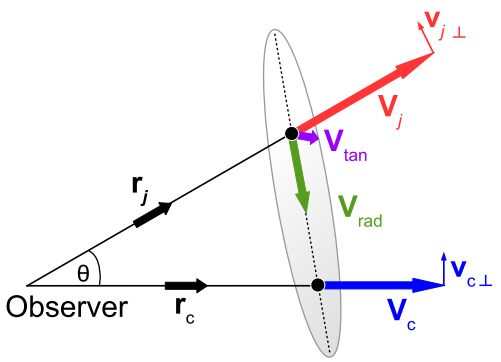

Model	Components set to zero
Minor	$v_{1,\perp}$ and $v_{2,\perp}$
Major	$v_{c,\perp}$ and v_{tan}

Fig. 4. Relative location and motion of a galaxy, j, at distance r_j from an observer with respect to the centre of mass at distance r_c. The vector $\boldsymbol{v}_j$ represents the line-of-sight velocity of galaxy j, while $\boldsymbol{v}_c$ is the line-of-sight velocity of the barycentre. The angle θ is measured between $\boldsymbol{r}_j$ and $\boldsymbol{r}_c$. The prerequisites for the two infall models to accurately describe the radial velocity, $\boldsymbol{v}_{rad}$, are listed in the table.

to M 81. The closest is on the left; the farthest is on the right. The major infall model yields velocity amplitudes larger than 1000 km/s for 13 of the galaxies, which is why these values are not shown in the plot. While this figure was produced using the barycentre on the connection line between M 81 and M 82 and taking into account the observers' motion within the Local Group, we systematically investigate the impact of each of these assumptions on the infall models and on the Hubble flow fit in the next section.

5. Hubble flow fit

5.1. Fitting function and uncertainty propagation

With the infall velocities set up in Sect. 4 and the independently determined distances for all galaxies to the barycentre of the M 81 complex, denoted as $\|\boldsymbol{r}_{cj}\|_2 \equiv r_{cj}$ for each galaxy j, we plot the Hubble diagram for the M 81 group. For the Hubble flow fit to the Hubble diagram, we used the approximation from Peirani & de Freitas Pacheco (2006, 2008), Peñarrubia et al. (2014), Benisty & Del Popolo (2025):

$$\left|\boldsymbol{v}_{\mathrm{inf}\,j}\right| = \left|\boldsymbol{v}_{\mathrm{inf}\,j}\right|\left(r_{cj}\right) = \kappa H_0 r_{cj} - 1.1\sqrt{\frac{GM}{r_{cj}}}, \tag{7}$$

in which κ is a scaling factor in front of the Hubble constant H_0, G is the gravitational constant, and M is the total mass of the M 81 complex. In Peñarrubia et al. (2014), $\kappa \approx 1.4$, but varying values can be found in the literature, depending on the embedding background (Del Popolo et al. 2021; Del Popolo & Chan 2022). The fit thus yields H_0 and M from the infall velocities and the observed distances of all galaxies in the M 81 complex. The turnaround, $|\boldsymbol{v}_{\mathrm{inf}\,j}| = 0$, from Eq. (7) yields the known enclosed mass relation from Sandage (1986):

$$M = 1.8 \cdot 10^{12}\left(\frac{H_0}{70\,\mathrm{km/s/Mpc}}\right)^2\left(\frac{r_{ta}}{1\,\mathrm{Mpc}}\right)^3, \tag{8}$$

where r_{ta} is the turnaround distance of the structure.

Before we determined the best-fit H_0 and M, we investigated the impact of shifting the barycentre from M 81 to the point on the connection line between M 81 and M 82 determined in Sect. 4.2, as well as the impact that the corrections to the velocities for our motion in the Local Group detailed in Sect. 4.1 have. Since the Hubble flow also starts at a specified minimum distance from the barycentre, d_{min}, and extends to a maximum distance from the barycentre, d_{max}, the impact of these fitting parameters also needs to be investigated. For all analyses, we only employed the 58 galaxies that have the TRGB-based distances with the highest measurement precision out of all of the distance-measure methods.

In order to obtain the most realistic estimates of uncertainties, for each galaxy j that has a TRGB-based distance we drew 10 000 samples from a Gaussian distribution around the observed r_j and $v_{hel\,j}$, respectively, using $\Delta r_j = 0.05\,r_j$ and $\Delta v_{hel\,j}$ as widths. Subsequently, for each of the 10 000 sample datasets containing 58 galaxies, we determined the barycentre (either the

position of M 81 in this sample dataset, or the point on the connection line between the M 81 and M 82 sample detailed in Sect. 4.2). We then calculated the infall velocities of all 58 galaxies towards this barycentre for each of the 10 000 datasets. In this way, the standard deviation of the 10 000 samples around the mean distance of galaxy j to the barycentre serves as the confidence bound on the TRGB-based distances. For the minor infall velocity, we analogously set up its confidence bound based on the standard deviation around the mean minor infall velocity for each galaxy. For the major infall velocity, we needed to set up its confidence bound based on the 0.159 and 0.841 quantiles, which corresponds to the 1σ bounds around the mean. This is the case due to chance alignments between galaxies and the barycentre that cause the denominator in Eq. (6) to diverge.

5.2. Impact of parameter dependencies and assumptions

We systematically show the impact of the velocity corrections, the choice of the barycentre, and data cuts on the Hubble flow fit. The Hubble diagrams in Fig. 5 were generated for the four combinations, from top to bottom: (1) M 81 as the barycentre and $v_{\rm hel}$ as the basis to calculate the infall velocities, (2) the point on the connection line between M 81 and M 82 as the barycentre and $v_{\rm hel}$ for the calculation of the infall velocities, (3) M 81 as the barycentre and $v_{\rm LG}$ to determine the infall velocities, and (4) the point on the connection line between M 81 and M 82 as the barycentre and $v_{\rm LG}$ to calculate the infall velocities. For each of these four options, the minor or major infall model was used to calculate the infall velocities, as is shown on the left side of Fig. 5 in blue and on the right side in red, respectively. The uncertainties in the three-dimensional distance between all galaxies and the barycentre, $\|\boldsymbol{r}_{{\rm c}\,j}\|_2$, and in the infall velocities, $\left|\boldsymbol{v}_{{\rm inf}\,j}\right|$, were obtained in the manner detailed in Sect. 5.1, based on 10 000 samples. Increasing the amount of samples to 100 000 does not change the size of the error bars significantly.

In addition, we also investigated variations in the minimum distance from the barycentre, $d_{\rm min}$, to start the Hubble flow fit. Karachentsev & Kashibadze (2006) chose 0.5 Mpc as fiducial value. We additionally show Hubble flow fits starting at 0.75 Mpc and 1 Mpc distance to the barycentre. Due to the instability of the major infall model, we also tested the impact of upper bounds on the major infall velocity, using an upper absolute value of 700 km/s and 500 km/s.

All Hubble flow fits to the data given the uncertainties calculated by the sampling were obtained by total least squares using a SVD. This is possible because H_0 and M are both larger than zero and Eq. (7) is a linear function in H_0 and $\sqrt{M}$ as parameters. The lines (solid, dashed, dotted) in Fig. 5 show the resulting Hubble flow fits for the varying $d_{\rm min}$. The corresponding best-fit values for κH_0 and M are listed in Table C.1 in the appendix. From the figure, it is already clear that the minor infall model yields very robust Hubble flow fits, irrespective of $d_{\rm min}$. We also note that the variance around the Hubble flow is decreased when using the refined barycentre position and velocity between M 81 and M 82 and additionally applying velocity corrections for our motion in the Local Group. The same trends can also be read off the plots for the major infall model; however, with much less robust results due to a diverging denominator in Eq. (6) when galaxies are sub-optimally aligned with the barycentre such that the denominator becomes small. Table C.1 even lists unphysical, negative values for κH_0 and unrealistically large masses, M. To further investigate the robustness of the major infall model, we studied the impact of different cuts on $\|\|\boldsymbol{v}_{{\rm inf}\,j}\|_2$, as is shown in the central and bottom tables of Table C.1. Since both velocity cuts, 700 km/s and 500 km/s, lead to overestimated H_0 and M values, the larger spread of the major infall velocities compared to the minor infall velocities causes the less stable Hubble flow fit. From these results, we also conclude that the major infall model, except for the unphysical negative H_0-values, can be considered as an upper bound on κH_0 and M. Establishing the minor infall model as a lower bound for both parameters is motivated from Benisty & Mota (2025): The Illustris TNG50 simulation analysed in their Fig. 3 shows that the starting velocity for the Hubble flow fit is above the true one and the slope for the minor infall model is smaller than the one of the simulated velocities. This result found in mock data seems to be valid for observations based on the results shown in Fig. 6.

Given that at least 20 galaxies are available to perform the Hubble flow fits, the resulting parameters are expected to differ only slightly from those obtained with ordinary least squares. As ordinary least squares only allows for shifts in the velocity direction, it yields increased stability compared to the de-regularizing total least squares, which allows for shifts in both distance and velocity directions. Therefore, our best-fit Hubble flow parameters are determined by ordinary least squares in the next section.

5.3. Best-fit Hubble flow fit

Our final Hubble flow fit was performed using the barycentre between M 81 and M 82 and accounting for velocity corrections in the Local Group. In addition, we enforced $\|\boldsymbol{v}_{{\rm inf}\,j}\|_2 \in [-500, 500]$ km/s. The uncertainties on the distances to the barycentre and infall velocities were again determined in the manner detailed in Sect. 5.1. Galaxies with uncertainties larger than 10% on the infall velocity and 100% on the distance to the barycentre were omitted.

To test the impact of the embedding environment, we performed two fits for each infall model: one including the last two galaxies around 5 Mpc distance from M 81, choosing $d_{\rm max} = 7$ Mpc, and one excluding those galaxies, $d_{\rm max} = 4$ Mpc. Within these boundaries, there are five satellite galaxies that have $\theta_1 < 0$ for M 81 as their major disturber (large black points in Fig. 5).

We fitted Eq. (7), the model-based infall velocity, $|\boldsymbol{v}^{\rm (mod)}_{{\rm inf}\,j}|$, to the infall velocity inferred from the measurements, $|\boldsymbol{v}^{\rm (obs)}_{{\rm inf}\,j}|$, via a χ^2-optimisation with

$$\chi^2 = -\sum_{j=1}^{n_{\rm g}} \frac{\left(|\boldsymbol{v}^{\rm (mod)}_{{\rm inf}\,j}| - |\boldsymbol{v}^{\rm (obs)}_{{\rm inf}\,j}|\right)^2}{2\sigma_j^2}, \tag{9}$$

in which σ_j is given by adding the squared uncertainties in the infall model velocity and the linear propagation of uncertainty of the distance uncertainty:

$$\sigma_j^2 = \left(\Delta|\boldsymbol{v}^{\rm (obs)}_{{\rm inf}\,j}|\right)^2 + \left(\frac{\partial|\boldsymbol{v}^{\rm (mod)}_{{\rm inf}\,j}|}{\partial r_{{\rm c}\,j}}\Delta r_{{\rm c}\,j}\right)^2. \tag{10}$$

To constrain the best-fit values for κH_0 and M, a nested sampling was used with the `PolyChord` package (Handley et al. 2015). We used a uniform prior for $\kappa H_0 \in [10, 200]$ km/s/Mpc and $M \in [0.01, 8]\times10^{12}\,M_\odot$. Fig. 6 is plotted with the `getdist` package (Lewis 2025) and shows the resulting confidence regions for the minor (blue) and the major infall models (red), once for $d_{\rm max} = 4$ Mpc (pale regions) and once for $d_{\rm max} = 7$ Mpc (intensely coloured regions). The table underneath the corner plot lists the best-fit values for κH_0 and M and their 1σ confidence intervals, as well as an estimate for H_0 when fixing

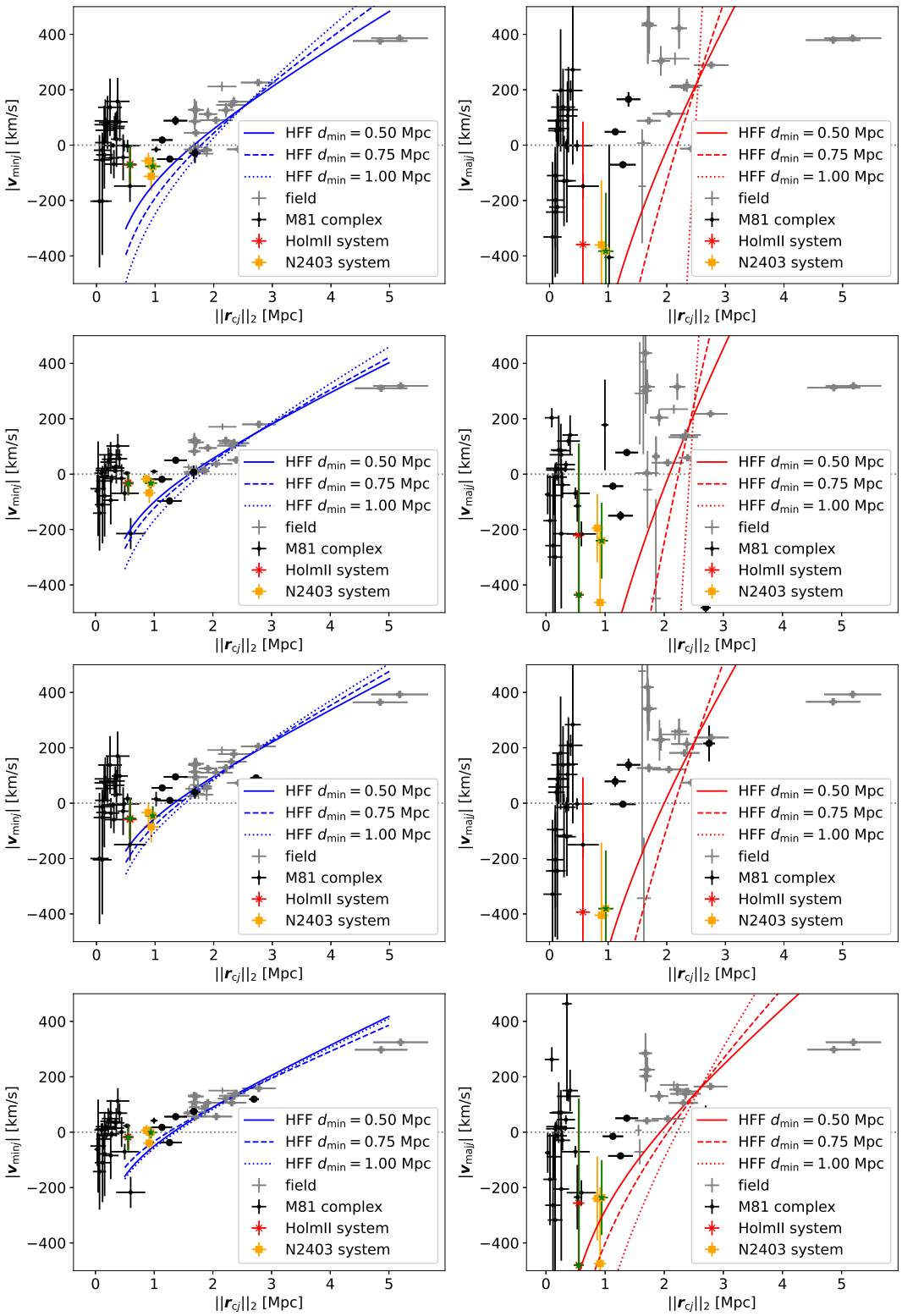

Fig. 5. Dependence of the Hubble flow fit on the minimum distance from the barycentre for the minor (left column) and major infall models (right column). The first and third rows have M 81 as the centre of mass. The second and fourth row use the barycentre located on the connection line between M 81 and M 82. The first and second row use v_{hel}. The third and fourth row use v_{LG}. For the major infall model, velocities up to a maximum value of 700 km/s were included in the fit.

$\kappa = 1.4$. Moreover, we report the best-fit values for M and H_0 in which minor and major infall models coincide within their 2σ confidence bounds, denoted as the 'overlap' model.

From the table, we read off that excluding the outmost two galaxies from the fit, the best-fit M and κH_0 are increased compared to the fit including these galaxies. Given that these two galaxies, DDO 87 and UGC05423, both have $\Theta_1 < 0$ for their major disturbers, it is likely that these galaxies belong to the Hubble flow of the M 81 complex. While one could choose a different κ to account for the varying d_{max} when determining H_0,

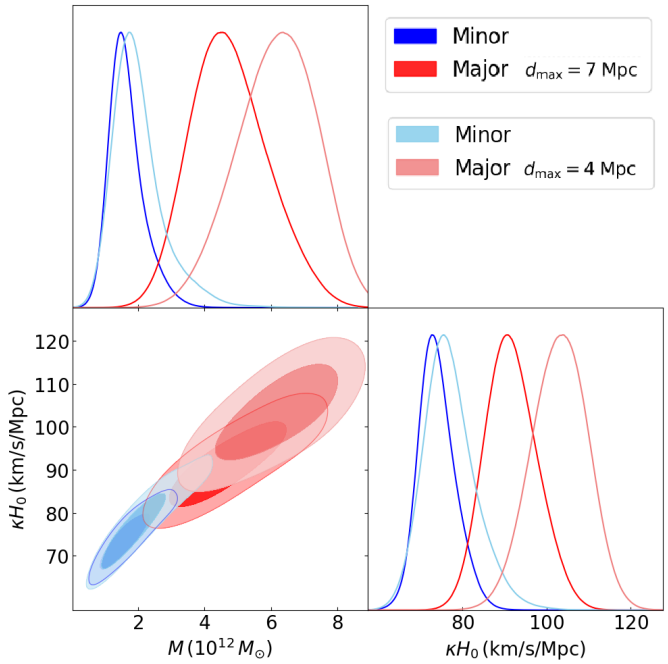

Fig. 6. Confidence intervals on κH_0 and M for the Hubble flow fit using the minor (blue) and major infall models (red) with respect to the barycentre between M 81 and M 82, a starting distance for the fit of $d_{min} = 0.5$ Mpc and the two maximum distances of galaxies included in the fit of $d_{max} = 4$ Mpc (omitting the two farthest galaxies) and $d_{max} = 7$ Mpc (including all galaxies in the dataset). To obtain a robust fit, galaxies with $\|\boldsymbol{v}_{majj}\|_2 > 500$ km/s were excluded. The overlap model yields the best-fit parameter values from the 2σ regions where the minor and major infall models coincide.

Table 2. The values for the posterior distributions.

Model	d_{max} [Mpc]	M $[10^{12}\,M_\odot]$	κH_0 [km/s/Mpc]	$H_0\,(\kappa = 1.4)$ [km/s/Mpc]
Minor	4	2.37 ± 0.91	81.4 ± 6.6	58.1 ± 4.7
Major	4	6.42 ± 1.08	108.5 ± 6.3	77.5 ± 4.5
Minor	7	1.72 ± 0.54	75.9 ± 4.4	54.2 ± 3.1
Major	7	5.04 ± 1.20	97.1 ± 6.3	69.4 ± 4.5
Overlap	7	2.28 ± 0.49	–	62.6 ± 5.4

we shall see in Sect. 7 that the increased mass, particularly for the major infall model, becomes inconsistent with other mass estimation approaches, hinting at the necessity to include these galaxies in the Hubble flow fit.

For the quality of fit, Fig. 7 shows the Hubble-flow fits (Eq. (7)) for the minor (top panel) and major (bottom panel) infall models for the 58 galaxies with TRGB-based distances in our dataset. The fits are shown for two different maximum distances: $d_{max} = 7$ Mpc (solid lines) and $d_{max} = 4$ Mpc (dashed lines). The shaded regions around the fits indicate 1σ credible intervals, obtained via linear propagation of uncertainties for the standard deviations of κH_0 and M listed in Table 6.

6. Dynamical mass estimates

In order to investigate the consistency of the Hubble flow fit and the mass inferred from it, we compare our results obtained in

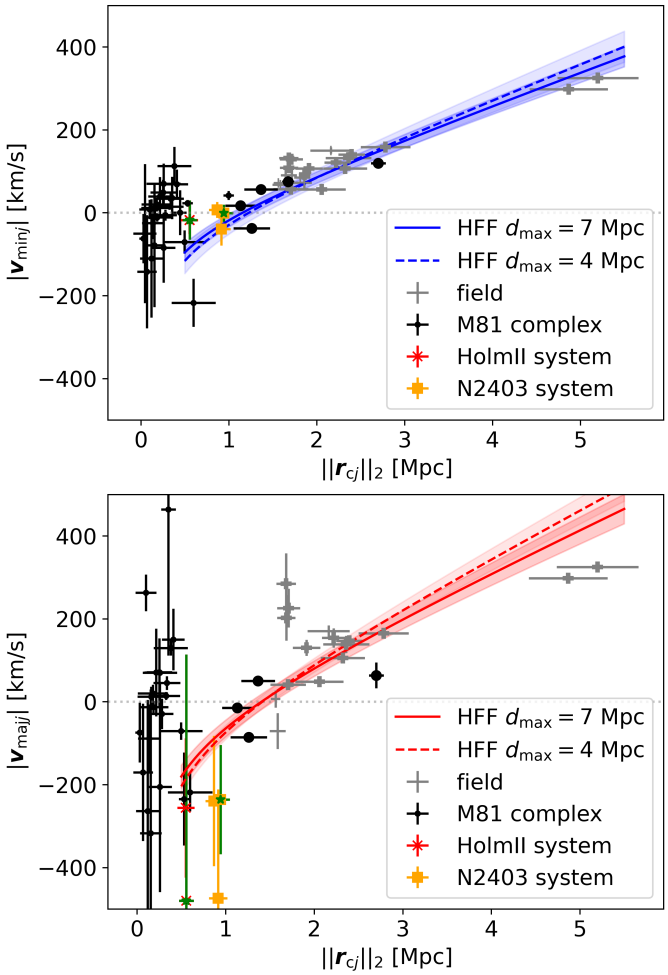

Fig. 7. Hubble flow fits (Eq. (7)) for the minor (top) and major infall models (bottom) with a starting distance for the fit of $d_{min} = 0.5$ Mpc and a maximum distance of galaxies included in the fit of $d_{max} = 7$ Mpc (solid lines) and $d_{max} = 4$ Mpc (dashed lines). The 1σ confidence bounds around both fits are based on linear propagation of uncertainties for the standard deviations of κH_0 and M as given in the table below Fig. 6.

Sect. 5 with masses inferred from the virial theorem and the projected-mass-method.

6.1. Hubble-flow-fit mass

As is listed in the table below Fig. 6, the minor infall model yielded a low mass and Hubble constant, while the major infall model obtained systematically higher values for M and H_0. However, the inferred parameter values overlap within their 2σ confidence bounds. From the overlapping confidence regions, we infer a common mass of $M = (2.28 \pm 0.49) \times 10^{12}\,M_\odot$, and $H_0 = (62.6 \pm 5.4)$ km/s/Mpc. Our best-fit H_0-values are thus in agreement with Planck Collaboration VI (2020) within 1σ, yet they are also in agreement with Riess et al. (2022) within 2σ.

6.2. Projected mass

As a second mass estimate, we determined the projected mass, M_{proj}, following the formalism of Bahcall & Tremaine (1981),

An & Evans (2011):

$$M_{\rm proj} = \frac{\alpha_{\rm proj}}{G}\frac{1}{n_{\rm g}}\sum_{j=1}^{n_{\rm g}} v_j^2 R_{{\rm c}j}, \tag{11}$$

in which each galaxy's line-of-sight velocity is given as v_j and $R_{{\rm c}j} \equiv r_{\rm c}\theta_{{\rm c}j}$ is the physical, projected two-dimensional distance between galaxy j and the barycentre. As usual, G is the gravitational constant and $\alpha_{\rm proj}$ is a geometric factor that encapsulates projection and anisotropy effects. For an isotropic velocity distribution, we adopted $\alpha_{\rm proj} = 16/\pi$. Inserting the $v_{\rm LG}$ as velocities for all $n_{\rm g} = 58$ galaxies that have TRGB-based distances and the position of the barycentre between M 81 and M 82 as $r_{\rm c}$, the mass of the M 81 complex becomes $M_{\rm proj} = (2.74 \pm 0.36) \times 10^{12}\,M_\odot$. Its uncertainty was inferred from a linear propagation of uncertainties from the measurement uncertainties (see Table A.1).

6.3. Virial mass

This estimator assumes that $n_{\rm vir}$ satellite galaxies act as test particles in virial equilibrium in a common potential, such that $M_{\rm vir}$ reflects the total gravitationally bound mass within the region sampled by the tracers:

$$M_{\rm vir} = \alpha_{\rm vir}\frac{\sigma_{\rm v}^2 r_{\rm G}}{G}, \quad \text{with} \quad r_{\rm G} = n_{\rm vir}\left(\sum_{j=1}^{n_{\rm vir}}\frac{1}{r_{0j}}\right)^{-1}, \tag{12}$$

in which $\sigma_{\rm v}$ denotes the velocity dispersion of the $n_{\rm vir}$ galaxies and r_{0j} is the three-dimensional distance between the centre of the virial volume and galaxy j (Bahcall & Tremaine 1981; Heisler et al. 1985; An & Evans 2011; Tully 2015a). As usual, G is the gravitational constant. The dimensionless coefficient, $\alpha_{\rm vir}$, represents a geometric form factor accounting for an underlying dark-matter distribution and velocity anisotropies. For instance, $\alpha_{\rm vir} = 3$ corresponds to isotropic orbits in an isothermal sphere, $\alpha_{\rm vir} = 2.6$ to isotropic velocities in a Navarro-Frenk-White profile, and $\alpha_{\rm vir} = 2.4$ to specific anisotropy models (Limber & Mathews 1960; Bahcall & Tremaine 1981).

Modelling the M 81 complex with a single, spherically symmetric potential is a good approximation only for radii much larger than the virial radius. Since the core is better approximated as a binary system with M 81 and M 82 as the most massive galaxies (see also Sect. 4.2), we generalised the virial mass estimate to a binary system according to Diaz et al. (2014) and Benisty et al. (2024). To do so, we replaced r_{0j} in Eq. (12) with the mass-weighted average

$$r_{\rm G} = n_{\rm vir}\left(\sum_{j=1}^{n_{\rm vir}}\frac{m_{\rm M\,81}}{r_{{\rm M\,81}j}} + \frac{1-m_{\rm M\,81}}{r_{{\rm M\,82}j}}\right)^{-1}, \tag{13}$$

in which each satellite galaxy, j, has a distance of $r_{{\rm M\,81}j}$ to the centre of M 81 and $r_{{\rm M\,82}j}$ to M 82. The mass ratio is $m_{\rm M\,81} \equiv M_{\rm M\,81}/(M_{\rm M\,81} + M_{\rm M\,82})$ with the masses of M 81 and M 82 being $M_{\rm M\,81}$ and $M_{\rm M\,82}$, based on their luminosity as in Sect. 4.2. Then, the velocity dispersion, $\sigma_{\rm v}$, was determined with respect to the barycentre between M 81 and M 82 from Sect. 4.2. To encompass uncertainties in the dark matter distribution, we adopted a broad uniform prior of $\alpha_{\rm vir} \in [2, 4]$. For the $n_{\rm vir} = 36$ member galaxies bound to the M 81 complex, we estimated $\sigma_{\rm v} = (106 \pm 4)$ km/s from the stable minor infall model velocities multiplied by $\sqrt{3}$, which is in good agreement with the previous best-fit value of $\sigma_{\rm v} = 102$ km/s obtained in Wagner & Benisty (2025). Moreover, $r_{\rm G} = (0.41 \pm 0.04)$ Mpc, which is close to $d_{\rm min} = 0.5$ Mpc as the starting radius for the Hubble flow fit, from the data in Table A.1 to arrive at $M_{\rm vir} = (3.11 \pm 0.69) \times 10^{12}\,M_\odot$.

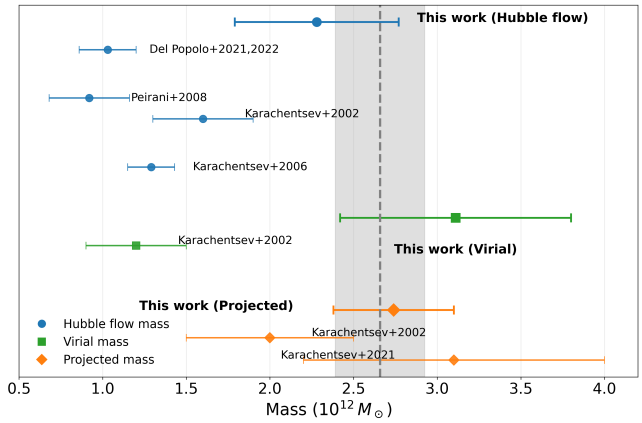

Fig. 8. Comparison of M 81-group mass estimates of this work using the Hubble flow, virial, and projected mass methods (blue circles, green squares, and orange diamonds, respectively), together with mass estimates from the literature. The vertical dashed grey line and shaded band indicate the weighted mean and 1σ uncertainty of the three estimates of this work. For comparison, literature values are shown: Hubble flow analyses by Del Popolo et al. (2021), Del Popolo & Chan (2022), Peirani & de Freitas Pacheco (2008), and Karachentsev et al. (2002), Karachentsev & Kashibadze (2006); virial and projected pass estimates from Karachentsev et al. (2002); and the most recent projected mass by Karachentsev & Kashibadze (2021).

7. Conclusion

We employed precise TRGB-based distances for nine previously unmeasured or imprecisely measured galaxies to determine the dynamics of M 81 complex. This expanded dataset, now comprising of 58 galaxies with high-precision TRGB-based distances, has allowed us to perform a robust dynamical analysis of the group's core and its embedding in the local Hubble flow.

Despite the increased amount of data and the improved precision of it, finding an alignment of the M 81 complex with the supergalactic SGX-SGY-plane still depends on a few galaxies between the second turnaround radius of ca. 0.23 Mpc and the virial radius of ca. 0.41 Mpc. The alignment, however, becomes robust beyond the virial radius, which formed the outer limit of the study by Müller et al. (2024). Our study in Sect. 3 revealed the filamentary structure around the M 81 group in a volume of about 5 Mpc radius. Hence, the filaments found are on a scale larger than the satellite plane of Müller et al. (2024) and on a smaller scale than the filaments of Raj et al. (2024).

Within this environment, our dataset contains a Hubble flow of more than 30 galaxies for which we performed a Hubble flow fit. Under the assumption that light traces mass, we demonstrate that this Hubble flow fit is best performed from the barycentre of the group determined as the point on the connection line between the two most luminous galaxies in the group, M 81 and M 82. Incorporating more galaxies, such as NGC 3077 and N 2976, does not change the position or line-of-sight velocity of the barycentre further for the given measurement precision. Moreover, it is important to account for the observers' motion in the Local Group to alleviate the variance in the infall velocities of the satellite galaxies onto the barycentre of the M 81 complex.

We also investigated the impact of the satellite selection for the Hubble flow fit. Both models systematically increase their best-fit M and H_0 values when restricting the fitting region to a maximum distance of 4 Mpc from the barycentre. Identifying the most distant galaxies on the Hubble flow is thus not only

important to obtain an accurate value for H_0, but also for M. Varying the starting distance for the Hubble flow fit, we find that the minor infall model yields more robust mass and H_0 values for different starting and ending points of the fit than the major infall model, which is highly sensitive to these choices. In general, analogously to Wagner & Benisty (2025), we find that the major infall model shows a larger dispersion in the infall velocities and that the minor and major infall models can be considered as lower and upper bounds for the true Hubble flow fit parameters. We therefore determined the Hubble flow fit parameters, $M_{\rm HFF} = (2.28 \pm 0.49) \times 10^{12}\,M_\odot$ and $H_0 = (62.6 \pm 5.4)$ km/s/Mpc, from the overlapping 2σ bounds on both infall models. For the latter, we set $\kappa = 1.4$ similarly to Peñarrubia et al. (2014), fixing the degeneracy between the background embedding and H_0 in the Hubble flow formula. Choosing smaller κ, H_0 can be larger, shifting the agreement from Planck Collaboration VI (2020) to Riess et al. (2022). Our H_0 value with an imprecision of about 8% is not precise enough to alleviate the Hubble tension, but it is consistent with prior works inferring H_0 in the local Universe, using TRGB-based distances (see, for instance, Kim et al. (2020) for a similar result of a Hubble flow fit in the Virgo cluster and Adame et al. (2025) and references therein for a more details on other H_0-probes). Tully et al. (2023) also discuss the TRGB-zero-point calibrations and current disputes over it, potentially causing the discrepancy in Cepheid-based distances in the local volume.

Comparing the Hubble flow fit M of the entire M 81 complex with the virial and projected mass estimates based on our improved dataset, a more consistent picture emerges compared to prior work from the literature, as is summarised in Fig. 8. Analyses by Del Popolo et al. (2021), Del Popolo & Chan (2022), and Peirani & de Freitas Pacheco (2008) obtained masses from a Hubble flow fit close to $10^{12}\,M_\odot$, while slightly higher values were reported by Karachentsev et al. (2002) and Karachentsev & Kashibadze (2006). Using alternative approaches, such as the virial theorem and projected mass estimators, Karachentsev et al. (2002) and Karachentsev & Kashibadze (2021) obtained comparable or higher masses. Overall, the literature suggested that the M 81 system has a total mass of the order of $(1{-}2) \times 10^{12}\,M_\odot$, consistent with expectations for a relatively low-mass, nearby galaxy group dominated by a few large spirals. Yet, previous mass estimates were based on even sparser datasets and only used the minor infall model, which jointly led to systematically lower mass estimates, with masses around $10^{12}\,M_\odot$, than the values obtained in this work, $M_{\rm proj} = (2.74 \pm 0.36) \times 10^{12}\,M_\odot$ and $M_{\rm vir} = (3.11 \pm 0.69) \times 10^{12}\,M_\odot$. The latter, however, is subject to a very large uncertainty based on the known logarithmic divergence of the harmonic radius, $r_{\rm G}$ (Bahcall & Tremaine 1981).

The consistency among the three mass estimation techniques in our analysis suggests that the higher mass is not an artefact of a single estimator, but rather reflects a genuine physical difference that may arise from updated kinematics, improved distance measurements, and a more accurate treatment of the system's gravitational potential. The higher inferred masses imply that M 81 may be dynamically more evolved and more strongly bound than earlier studies indicated, with potential implications for its satellite population and the distribution of dark matter within the group. The already planned HST observations in the SNAP 18070 programme of eight galaxies with poorly constrained distances, UGC06451, KKH30, SMDG0956+82, KDG162, Dw1907+63, Dw1940+64, Dw1559+46, and Dw1735+57, in the upcoming C 33 cycle will certainly bring further clarity and enable our results to be checked in the near future.

Data availability

Movie associated to Fig 3 is available at https://www.aanda.org

Acknowledgements. DB is supported by the Minerva Stiftung Gesellschaft für die Forschung mbH. This article is based on work from the COST Action CA21136 – "Addressing observational tensions in cosmology with systematics and fundamental physics" (CosmoVerse) and the Cost Action CA23130 – "Bridging high and low energies in search of quantum gravity" (BridgeQG), supported by COST (European Cooperation in Science and Technology). IK is supported by the Russian Science Foundation grant No 24-12-00277, "Cosmography of the Local Volume of the Universe within 15 megaparsecs".

References

Adame, A. G., Aguilar, J., Ahlen, S., et al. 2025, JCAP, 2025, 021
An, J. H., & Evans, N. W. 2011, MNRAS, 413, 1744
Anand, G. S., Tully, R. B., Rizzi, L., Shaya, E. J., & Karachentsev, I. D. 2019, ApJ, 880, 52
Bahcall, J. N., & Tremaine, S. 1981, ApJ, 244, 805
Benisty, D., & Del Popolo, A. 2025, ArXiv e-prints [arXiv:2510.11382]
Benisty, D., & Mota, D. 2025, A&A, 698, A43
Benisty, D., Chaichian, M. M., & Tureanu, A. 2024, Phys. Lett. B, 858, 139033
Del Popolo, A., & Chan, M. H. 2022, ApJ, 926, 156
Del Popolo, A., Deliyergiyev, M., & Chan, M. H. 2021, Phys. Dark Universe, 31, 100780
Diaz, J. D., Koposov, S. E., Irwin, M., Belokurov, V., & Evans, N. W. 2014, MNRAS, 443, 1688
Handley, W. J., Hobson, M. P., & Lasenby, A. N. 2015, MNRAS, 450, L61
Heisler, J., Tremaine, S., & Bahcall, J. N. 1985, ApJ, 298, 8
Karachentsev, I. D., & Kashibadze, O. G. 2006, Astrophysics, 49, 3
Karachentsev, I., & Kashibadze, O. 2021, Astron. Nachr., 342, 999
Karachentsev, I. D., & Makarov, D. A. 1996, AJ, 111, 794
Karachentsev, I. D., & Makarov, D. I. 1999, IAU Symp., 186, 109
Karachentsev, I. D., Dolphin, A. E., Geisler, D., et al. 2002, A&A, 383, 125
Karachentsev, I. D., Kashibadze, O. G., Makarov, D. I., & Tully, R. B. 2009, MNRAS, 393, 1265
Karachentsev, I. D., Makarov, D. I., & Kaisina, E. I. 2013, AJ, 145, 101
Kim, Y. J., Kang, J., Lee, M. G., & Jang, I. S. 2020, ApJ, 905, 104
Kourkchi, E., Courtois, H. M., Graziani, R., et al. 2020, AJ, 159, 67
Lewis, A. 2025, JCAP, 08, 025
Limber, D. N., & Mathews, W. G. 1960, ApJ, 132, 286
Makarov, D., & Karachentsev, I. 2011, MNRAS, 412, 2498
Makarov, D., Makarov, D., Makarova, L., & Libeskind, N. 2025, A&A, 698, A178
McCall, M. L. 2014, MNRAS, 440, 405
Müller, O., Heesters, N., Pawlowski, M. S., et al. 2024, A&A, 683, A250
Peebles, P. J. E. 2023, MNRAS, 526, 4490
Peirani, S., & de Freitas Pacheco, J. A. 2006, New Astron., 11, 325
Peirani, S., & de Freitas Pacheco, J. A. 2008, A&A, 488, 845
Peñarrubia, J., Ma, Y.-Z., Walker, M. G., & McConnachie, A. 2014, MNRAS, 443, 2204
Planck Collaboration VI. 2020, A&A, 641, A6
Raj, M. A., Awad, P., Peletier, R. F., et al. 2024, A&A, 690, A92
Riess, A. G., Yuan, W., Macri, L. M., et al. 2022, ApJ, 934, L7
Sandage, A. 1986, ApJ, 307, 1
Shaya, E. J., Tully, R. B., Hoffman, Y., & Pomarède, D. 2017, ApJ, 850, 207
Tully, R. B. 2015a, AJ, 149, 54
Tully, R. B. 2015b, AJ, 149, 171
Tully, R. B., Shaya, E. J., Karachentsev, I. D., et al. 2008, ApJ, 676, 184
Tully, R. B., Kourkchi, E., Courtois, H. M., et al. 2023, ApJ, 944, 94
Wagner, J., & Benisty, D. 2025, A&A, 698, A211

Appendix A: Observational datasets

Table A.1. The data used in this paper.

Name	α [deg]	δ [deg]	$v_{\rm hel}$ [km/s]	$\Delta v_{\rm hel}$ [km/s]	B [mag]	MD	Θ_1 [deg]	r [Mpc]	Method	HFF
MESSIER081*	148.889583	69.066667	-38	1	7.8	M 82	2.7	3.7	TRGB	
JKB83	148.956667	69.332500	56	10	19.7	M 81	5.3	3.7	mem	
KDG61em	149.281250	68.598333	116	21	18.8	M 81	4.5	3.7	mem	
KDG061*	149.261250	68.591667	221	3	15.2	M 81	4	3.66	TRGB	
NGC2976*	146.815000	67.913611	6	4	11	M 81	3	3.66	TRGB	
MESSIER082*	148.974583	69.682500	183	4	9.1	M 81	3.1	3.61	TRGB	
IKN*	152.024583	68.399167	-140	64	14.5	M 81	3	3.75	TRGB	
ClumpI	149.338333	68.715278	-165	18	19.8	M 82	3.2	3.6	mem	
ClumpIII	150.168333	68.660278	-121	20	19.8	M 82	3.1	3.6	mem	
KDG064*	151.757917	67.827500	-15	13	15.5	M 81	2.8	3.75	TRGB	
GARLAND*	150.925000	68.693333	43	17	16.8	N3077	3	3.82	TRGB	
F8D1*	146.196250	67.438611	-125	130	16.8	M 81	2.6	3.75	TRGB	
HIJASS 1021+68	155.250833	68.700000	46	1		M 81	2.5	3.7	mem	
HolmIX*	149.385000	69.043056	50	4	14.5	N3077	2.8	3.85	TRGB	
NGC3077*	150.837500	68.733889	19	4	10.6	M 81	2.3	3.85	TRGB	
d0958+66*	149.702083	66.849722	90	50	16	M 81	2.1	3.82	TRGB	
A0952+69*	149.370833	69.272222	99	2	16.8	M 81	1.9	3.93	TRGB	
d1028+70*	157.165417	70.233611	-114	50	16.2	M 81	1.8	3.84	TRGB	
d0944+71	146.143333	71.482500	-38	10	16.7	M 82	1.8	3.47	TRGB	
DDO078*	156.616250	67.656667	55	10	14.3	M 81	1.6	3.48	TRGB	
IC2574*	157.093333	68.416111	43	4	11.5	M 81	1.5	3.93	TRGB	
DDO082*	157.645833	70.619444	56	3	13.5	M 81	1.5	3.93	TRGB	
UGC05497*	153.201667	64.107500	150	50	15.6	M 81	1.4	3.73	TRGB	
HolmI*	145.134583	71.186389	139	1	13.6	M 81	1.3	4.02	TRGB	
KDG073	163.237917	69.545833	116	1	17.1	M 81	1.2	3.91	TRGB	
UGC04483	129.262500	69.775278	156	1	15	M 81	1	3.58	TRGB	
BK3N*	148.452083	68.969167	-40	20	18.8	M 81	1	4.17	TRGB	✓
DDO053	128.527083	66.179167	19	2	14.6	M 81	0.8	3.68	TRGB	
KDG052	125.983333	71.029444	116	2	16.4	HolmII	2	3.42	TRGB	
d0959+68	149.887917	68.656944	-186	44	18	M 81	0.7	4.27	TRGB	✓
HolmII	124.766667	70.714167	157	1	11.1	M 81	0.7	3.47	TRGB	
UGC06451	172.193333	79.601944	50	1	16.5	M 81	0.3	3.6	mem	
NGC2366	112.227500	69.205278	96	1	11.7	N2403	0.8	3.28	TRGB	
DDO44	113.547083	66.886111	213	25	15.6	N2403	2.3	3.21	TRGB	
NGC2403	114.214167	65.599444	125	17	8.8	DDO44	0.2	3.19	TRGB	
KKH37	101.940833	80.123889	11	7	16.4	M 81	0	3.44	TRGB	
NGC4236	184.180417	69.465556	-3	1	10.1	M 81	-0.2	4.41	TRGB	✓
KKH30	79.425000	81.624167	-67	20	17.5	M 81	-0.2	3.5	txt	
UGC06456	172.002500	78.991389	-94	2	14.3	M 81	-0.3	4.63	TRGB	✓
SMDG0956+82	149.054167	82.890000	-63	10	18.1	M 81	-0.4	2.6	NAM	
UGC06757	176.746250	61.334722	88	1	16.3	M 81	-0.4	4.61	TRGB	✓
KDG162	188.756667	58.385556	125	1	17.7	M 81	-0.5	2.8	NAM	
CamA	66.315000	72.805833	-54	2	14.8	IC342	0.7	3.56	TRGB	
NGC1560	68.207917	71.881111	-36	1	12.1	IC342	0.8	2.99	TRGB	✓
CamB	73.278750	67.099167	78	2	16.7	IC342	0.7	3.5	TRGB	
UGC06541	173.371250	49.238056	249	2	14.4	N4736	-0.6	4.23	TRGB	✓
UGC07298	184.119167	52.227222	174	2	16	N4736	-0.4	4.19	TRGB	✓
NGC3741	174.026667	45.285278	229	2	14.4	M 81	-0.7	3.22	TRGB	
Dw1245+6158	191.454167	61.968889	68	40	18.4			4.72	sbf	
DDO165	196.611667	67.704167	31	1	13.3	N4236	-0.6	4.83	TRGB	✓
NGC4068	181.010000	52.588611	210	2	13.2	N4736	-0.5	4.39	TRGB	✓
UGCA105	78.562917	62.580833	113	22	12.1	IC342	0.3	3.39	TRGB	
KKH22	56.235833	72.064444	30	10	17	IC342	1.3	3.12	TRGB	
NGC1569	67.704583	64.848056	-86	3	11.8	IC342	1.1	3.19	TRGB	
UGCA092	68.001250	63.613889	-95	2	15.2	N1569	1.8	3.22	TRGB	
UGCA086	59.956250	67.125278	72	5	13.5	IC342	1.1	2.98	TRGB	
IC0342	56.703750	68.095833	29	1	9.4	N1569	-0.1	3.28	TRGB	
MCG09-20-131	183.944583	52.387500	159	2	15.3	N4736	-0.4	4.61	TRGB	✓
UGC07242	183.530833	66.092222	66	2	14.6	N4605	-0.4	5.45	TRGB	✓
NGC3738	173.952500	54.522778	225	8	11.9	Dw1135+54	1.3	5.3	TRGB	✓
KK109	176.796667	43.671944	211	2	18.1	N4736	-0.3	4.51	TRGB	✓

Table A.1. continued.

Name	α [deg]	δ [deg]	$v_{\rm hel}$ [km/s]	$\Delta v_{\rm hel}$ [km/s]	B [mag]	MD	Θ_1 [deg]	r [Mpc]	Method	HFF
KK135	184.894583	58.042778	142	1	17.5	N4605	-0.2	5.46	TRGB	✓
NGC4605	190.001250	61.608056	151	17	10.9	M101	-1.1	5.55	TRGB	✓
UGC04879	139.009167	52.840000	-25	4	13.8	M31	-0.7	1.37	TRGB	✓
Dw1907+63	286.814167	63.385000	-147	10	18.3	M31	-1.1	2.4	NAM	
NGC6789	289.174167	63.972778	-140	9	13.8	M 81	-1.3	3.55	TRGB	✓
Grapes	178.023333	54.792222	223	1	18.3	N4258	-0.9	5.96	TRGB	✓
Dw1940+64	295.230833	64.758889	-59	10	18	M 81	-1.4	3.8	NAM	
Dw1559+46	239.760833	46.394444	77	1	17.2	M 81	-1.4	3.4	NAM	
Dw1735+57	263.894167	57.813056	43	1	17.1	M 81	-1.6	4.6	NAM	
DDO 087	162.402083	65.530556	340	6	15.2	N2787	-1.4	8.5	TRGB	✓
UGC05423	151.377500	70.364444	348	1	14.4	CKT1009+70	-0.5	8.87	TRGB	✓

Notes. M 81-group members with their name, co-ordinates on the sky (J2000), velocity with respect to the heliocentric frame, $v_{\rm hel}$, and its uncertainty, $\Delta v_{\rm hel}$, magnitude in the B-band, their 'major disturber' (MD) and tidal index to their MD, Θ_1, the distance to us as observers, r, and the method to determine the distance. The last column indicates if the galaxy was used for the Hubble flow fit (HFF) in Sect. 5.3. Rows are sorted according to their distance to M 81. Galaxies in the dataset by Müller et al. (2024) have a * after their name.

Table A.2. Galaxy positions used to analyse the embedding of the M 81 group into the surroundings in Sect. 3.

Name	α [deg]	δ [deg]	r [Mpc]
UGCA086	59.956250	67.125278	2.98
NGC1560	68.207917	71.881111	2.99
KKH22	56.235833	72.064444	3.12
NGC1569	67.704583	64.848056	3.19
NGC2403	114.214167	65.599444	3.19
DDO44	113.547083	66.886111	3.21
NGC3741	174.026667	45.285278	3.22
UGCA092	68.001250	63.613889	3.22
NGC2366	112.227500	69.205278	3.28
UGCA105	78.562917	62.580833	3.39
KDG052	125.983333	71.029444	3.42
KKH37	101.940833	80.123889	3.44
d0944+71	146.143333	71.482500	3.47
HolmII	124.766667	70.714167	3.47
DDO0 78	156.616250	67.656667	3.48
CamB	73.278750	67.099167	3.5
CamA	66.315000	72.805833	3.56
UGC04483	129.262500	69.775278	3.58
MESSIER082	148.974583	69.682500	3.61
KDG061	149.261250	68.591667	3.66
NGC2976	146.815000	67.913611	3.66
DDO 053	128.527083	66.179167	3.68
MESSIER081	148.889583	69.066667	3.7
UGC05497	153.201667	64.107500	3.73
F8D1	146.196250	67.438611	3.75
IKN	152.024583	68.399167	3.75
KDG064	151.757917	67.827500	3.75
d0958+66	149.702083	66.849722	3.82
GARLAND	150.925000	68.693333	3.82
d1028+70	157.165417	70.233611	3.84
HolmIX	149.385000	69.043056	3.85
NGC3077	150.837500	68.733889	3.85
KDG073	163.237917	69.545833	3.91
A0952+69	149.370833	69.272222	3.93

Table A.2. continued.

Name	α [deg]	δ [deg]	r [Mpc]
DDO 082	157.645833	70.619444	3.93
IC2574	157.093333	68.416111	3.93
HolmI	145.134583	71.186389	4.02
BK3N	148.452083	68.969167	4.17
UGC07298	184.119167	52.227222	4.19
UGC06541	173.371250	49.238056	4.23
d0959+68	149.887917	68.656944	4.27
NGC4068	181.010000	52.588611	4.39
KK109	176.796667	43.671944	4.51
MCG09-20-131	183.944583	52.387500	4.61
UGC06757	176.746250	61.334722	4.61
NGC3738	173.952500	54.522778	5.3
KK135	184.894583	58.042778	5.46
Grapes	178.023333	54.792222	5.96
DDO125	186.866124	43.534035	2.61
DDO 99	177.733649	38.914049	2.65
NGC4190	183.398633	36.632008	2.83
NGC4214	183.910646	36.348362	2.88
KDG 90	183.714621	36.190201	2.98
NGC4163	183.048224	36.219123	2.99
MADCASH-2	182.474314	35.423248	3.01
d0934+70	143.540382	70.150762	3.02
Dw0910+7326	137.607581	73.422892	3.21
BK6N	158.719439	66.011110	3.31
MADCASH J07	115.584970	65.397672	3.39
d0926+70	141.704262	70.493973	3.4
d0955+70	148.741602	70.361245	3.45
d1006+67	151.778768	67.191736	3.61
d0939+71	144.866137	71.337771	3.65
KDG063	151.226092	66.557001	3.65
KKH57	150.097580	63.231898	3.68
BK5N	151.241237	68.254032	3.7
d1041+70	160.448034	70.131159	3.7
d1009+68	152.221454	68.744898	3.73
KDG64	150.860512	68.112680	3.75
FM1	146.168642	68.750778	3.78
KK77	147.535550	67.509495	3.8
d0944+69	146.074789	69.173701	3.84
d1014+68	153.780248	68.726819	3.84
dw J0954+6821	148.555325	68.377482	3.87
HS117	155.426969	71.101060	3.96
d1005+68	151.241237	68.254032	3.98
d1015+69	153.815748	69.009308	4.07
J1228+4358	187.113727	43.999063	4.07
NGC4449	187.075854	44.094677	4.27
NGC4244	184.353019	37.832755	4.31
d1006+69	151.672831	69.949823	4.33
KK160	190.949440	43.695765	4.33
NGC4736	192.714679	41.159063	4.41
Cas1	31.509985	69.038416	4.51
IC3687	190.587934	38.530116	4.57
M94-dw2	192.701693	41.662077	4.7
DDO127	187.090133	37.253574	4.72
J1243+41	190.979521	41.463620	4.81
DDO126	186.729153	37.167847	4.97
UGCA281	186.604520	48.544859	5.7
Arp 211	189.312032	38.782555	6.14
NGC4144	182.468725	46.421076	6.89
UGC7639	187.472767	47.573257	7.14
KKH34	89.779274	73.425345	7.28
KDG101	184.781960	47.042640	7.28
DDO120	185.332830	45.805580	7.28

Table A.2. continued.

Name	α [deg]	δ [deg]	r [Mpc]
KK132	184.760320	47.767288	7.31
BTS132	185.884591	47.683344	7.4
NGC2787	139.820778	69.236964	7.48
NGC4242	184.375712	45.597763	7.62
NGC4258	184.651771	47.327853	7.66
NGC4618	190.396507	41.151496	7.66
UGC4998	141.217257	68.391474	8.24

Notes. Rows are sorted according to their distance to us. The first part of the table lists the 48 galaxies from Table A.1 used in this analysis, the second part lists 55 galaxies in the environment. As we only employ the galaxy locations, we do not list velocities here.

Appendix B: Propagation of statistical uncertainties

Given the uncertainties in the measured distances and heliocentric velocities, the propagation of errors is performed as follows: We correct the heliocentric velocities for the solar motion in the Local Group according to Eq. (2),

$$v_{\rm LG} = v_{\rm hel} + v_\odot\Big(\sin(b)\sin(b_\odot) + \cos(b)\cos(b_\odot)\cos(l-l_\odot)\Big)\,. \tag{B.1}$$

Due to the uncertainties in the apex parameters (Eq. 3), the linear uncertainty propagation

$$\Delta v_{\rm LG} = \sqrt{(\Delta v_{\rm hel})^2 + \left(\frac{\partial v_{\rm LG}}{\partial v_\odot}\Delta v_\odot\right)^2 + \left(\frac{\partial v_{\rm LG}}{\partial l_\odot}\Delta l_\odot\right)^2 + \left(\frac{\partial v_{\rm LG}}{\partial b_\odot}\Delta b_\odot\right)^2}\,, \tag{B.2}$$

with

$$\frac{\partial v_{\rm LG}}{\partial v_\odot} = \sin(b)\sin(b_\odot) + \cos(b)\cos(b_\odot)\cos(l-l_\odot)\,, \tag{B.3}$$

$$\frac{\partial v_{\rm LG}}{\partial l_\odot} = v_\odot\cos(b)\cos(b_\odot)\sin(l-l_\odot)\,, \tag{B.4}$$

$$\frac{\partial v_{\rm LG}}{\partial b_\odot} = v_\odot\left(\sin(b)\cos(b_\odot) - \cos(b)\sin(b_\odot)\cos(l-l_\odot)\right) \tag{B.5}$$

is just an approximation to realistic error bars, neglecting uncertainties in l and b as well.

Next, we equip distances to the barycentre with uncertainties. For the simplicity of notation, we define the measured distance to the barycentre and a galaxy j as $r_{\rm c} \equiv \|\boldsymbol{r}_{\rm c}\|_2$ and $r_j \equiv \|\boldsymbol{r}_j\|_2$, respectively. The angular distance between the barycentre and galaxy j is then $\theta_{{\rm c}j}$. In this notation, $r_{{\rm c}j} \equiv \|\boldsymbol{r}_{\rm c} - \boldsymbol{r}_j\|_2$, and its uncertainty are given by

$$r_{{\rm c}j} = \sqrt{r_{\rm c}^2 + r_j^2 - 2r_{\rm c}r_j\cos\theta_{{\rm c}j}}\,, \quad \Delta r_{{\rm c}j} = \sqrt{\left(\frac{r_{\rm c} - r_j\cos\theta_{{\rm c}j}}{r_{{\rm c}j}}\,\Delta r_{\rm c}\right)^2 + \left(\frac{r_j - r_{\rm c}\cos\theta_{{\rm c}j}}{r_{{\rm c}j}}\,\Delta r_j\right)^2}\,. \tag{B.6}$$

Uncertainties in $\theta_{{\rm c}j}$ are thus considered to be negligible again as in the previous step. Moreover, if the barycentre is determined as the mass-weighted positional average of several galaxies, the correlation between the uncertainties in $r_{\rm c}$ and r_j for those galaxies are neglected as well. Since these galaxies are located in the very centre of the M 81 complex and not relevant to constrain the second turnaround radius or the zero-velocity radius, a more precise error estimate is not important for this work.

Appendix C: Infall models and barycentre values

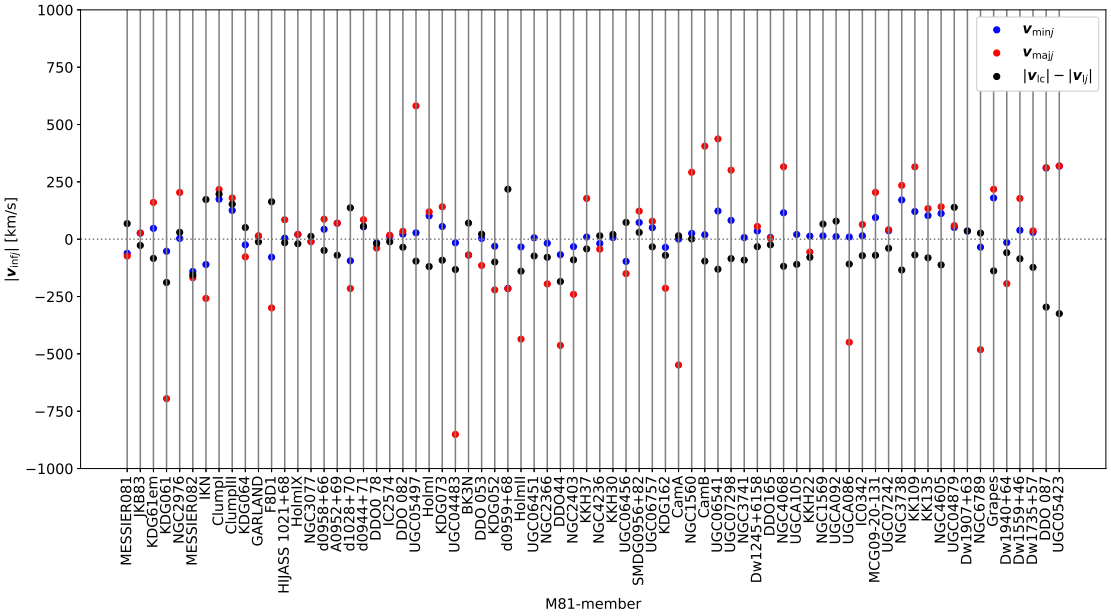

Fig. C.1. The infall velocities for all 72 galaxies in our dataset with respect to the barycentre of the M 81 complex located on the connection line between M 81 and M 82, including velocity corrections for the observers' motion within the Local Group. The galaxies are sorted with increasing distance from M 81 from left to right. The minor infall model velocities are marked in blue, major infall velocities in red, and just taking the difference between the line-of-sight velocities of the barycentre and a galaxy j are marked in black.

Table C.1. Hubble flow fit parameters for the minor (top row) and major infall model (centre, bottom row): κH_0 in km/s/Mpc (left) and M in $10^{12} M_\odot$ (right) with the singular values as uncertainties.

v	$d_{\min}$	Barycentre		v	$d_{\min}$	Barycentre	
	[Mpc]	M 81	M 81 & M 82		[Mpc]	M 81	M 81 & M 82
	0.5	119.5 ± 27.6	98.2 ± 25.4		0.5	12.5	7.6
$v_{\rm hel}$	0.75	138.2 ± 27.2	104.6 ± 24.6	$v_{\rm hel}$	0.75	20.8	9.9
	1	157.2 ± 27.0	117.2 ± 24.5		1	31.7	15.5
	0.5	104.1 ± 28.0	96.7 ± 26.6		0.5	4.8	4.1
$v_{\rm LG}$	0.75	112.3 ± 27.7	88.1 ± 26.0	$v_{\rm LG}$	0.75	7.0	2.8
	1	120.9 ± 27.5	95.6 ± 25.9		1	9.7	4.5

v	$d_{\min}$	Barycentre		v	$d_{\min}$	Barycentre	
	[Mpc]	M 81	M 81 & M 82		[Mpc]	M 81	M 81 & M 82
	0.5	327.3 ± 41.7	361.2 ± 39.9		0.5	172.6	228.2
$v_{\rm hel}$	0.75	466.1 ± 39.9	661.0 ± 38.6	$v_{\rm hel}$	0.75	434.3	946.1
	1	2525.9 ± 37.1	2178.0 ± 37.1		1	18570.0	13078.7
	0.5	303.2 ± 40.8	167.9 ± 35.2		0.5	132.4	39.2
$v_{\rm LG}$	0.75	440.2 ± 38.5	205.7 ± 32.6	$v_{\rm LG}$	0.75	363.0	71.1
	1	−502.8 ± 35.1	280.9 ± 27.1		1	1098.5	165.7

v	$d_{\min}$	Barycentre		v	$d_{\min}$	Barycentre	
	[Mpc]	M 81	M 81 & M 82		[Mpc]	M 81	M 81 & M 82
	0.5	312.1 ± 37.6	341.5 ± 38.6		0.5	170.2	197.5
$v_{\rm hel}$	0.75	421.3 ± 36.9	706.6 ± 37.3	$v_{\rm hel}$	0.75	374.7	1099.8
	1	924.9 ± 35.4	−5740.4 ± 35.5		1	2358.3	100123.3
	0.5	339.5 ± 37.6	156.4 ± 33.6		0.5	180.2	31.4
$v_{\rm LG}$	0.75	572.6 ± 36.8	192.4 ± 30.6	$v_{\rm LG}$	0.75	691.5	58.9
	1	−502.8 ± 35.1	280.9 ± 27.1		1	1098.5	165.7

Notes. For the major infall, cuts for $\|\boldsymbol{v}_{{\rm maj}j}\|_2 < 700$ km/s were applied (centre row) and $\|\boldsymbol{v}_{{\rm maj}j}\|_2 < 500$ km/s (bottom row). Mass uncertainties were much smaller than the precision for M stated here and are thus omitted.